

OPEN ACCESS

Ceria Entrapped Palladium Novel Composites for Hydrogen Oxidation Reaction in Alkaline Medium

To cite this article: Noam Ralbag *et al* 2020 *J. Electrochem. Soc.* **167** 054514

View the [article online](#) for updates and enhancements.



Ceria Entrapped Palladium Novel Composites for Hydrogen Oxidation Reaction in Alkaline Medium

Noam Ralbag,¹ Elena S. Davydova,² Meirav Mann-Lahav,² Peixi Cong,^{4,5} Jin He,¹ Andrew M. Beale,^{4,5} Gideon S. Grader,^{2,3,*} David Avnir,^{1,*} and Dario R. Dekel^{2,3,*,z}

¹Institute of Chemistry and the Center for Nanoscience and Nanotechnology, The Hebrew University of Jerusalem, Jerusalem 9190401, Israel

²The Wolfson Department of Chemical Engineering, Technion–Israel Institute of Technology, Haifa 3200003, Israel

³The Nancy & Stephan Grand Technion Energy Program (GTEP), Technion–Israel Institute of Technology, Haifa 3200003, Israel

⁴Department of Chemistry, University College of London, Gordon Street, London, WC1H 0AJ, United Kingdom

⁵Research Complex at Harwell, Rutherford Appleton Laboratory, Didcot OX110FA, United Kingdom

A new heterogeneous catalyst for hydrogen oxidation reaction (HOR), metallic palladium within which nanoparticles of ceria are entrapped, CeO₂@Pd, is described. Its preparation is based on a new materials methodology of molecular doping of metals. The metallic matrix, which engages the nanoparticles, is prepared in foam architecture, to ensure easy molecular diffusion. Characterization of the structural properties of the CeO₂@Pd composite using SEM, STEM, TEM, XRD, EXAFS and nitrogen adsorption reveals its morphological architecture, which leads to improved catalytic activity. In-situ electrochemical and H₂ temperature-programmed reduction (H₂-TPR) spectra provide direct experimental evidence of the weakening of Pd–H bond in the CeO₂@Pd composites, relative to pure (undoped) Pd catalysts. Gas diffusion electrodes based on the entrapped CeO₂@Pd catalysts demonstrated one order of magnitude higher activity than pure Pd analog in the HOR reaction in an alkaline medium.

© 2020 The Author(s). Published on behalf of The Electrochemical Society by IOP Publishing Limited. This is an open access article distributed under the terms of the Creative Commons Attribution 4.0 License (CC BY, <http://creativecommons.org/licenses/by/4.0/>), which permits unrestricted reuse of the work in any medium, provided the original work is properly cited. [DOI: 10.1149/1945-7111/ab74be]



Manuscript submitted October 22, 2019; revised manuscript received February 6, 2020. Published February 21, 2020. *This paper is part of the JES Focus Issue on Heterogeneous Functional Materials for Energy Conversion and Storage.*

Supplementary material for this article is available [online](#)

In spite of the remarkable development done in the anion exchange membrane fuel cells (AEMFCs), this technology is still hindered by several challenges, including the sluggish kinetics of the hydrogen oxidation reaction (HOR).^{1–12} To overcome this challenge, recent studies have focused their efforts in the development of Pd–CeO₂ composites, as a promising alternative to Pt-based catalysts for HOR.^{13,14} It was claimed that the use of ceria (CeO₂) promotes the electrooxidation of the hydrogen on the Pd catalyst surface by means of the bifunctional mechanism.^{1,2,12} In order to maximize this bifunctional effect, an intimate contact between Pd and ceria must be achieved. Several preparation methods have been proposed to enhance the Pd–ceria contact, among them, deposition of Pd onto ceria supports by wet chemistry method,^{14,15} ceria doping onto Pd nanoparticles by wet chemistry technique,¹⁶ and in situ co-deposition of Pd and ceria by flame pyrolysis¹⁷ have been reported.

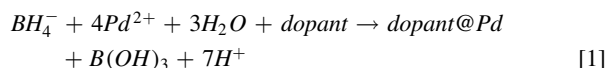
In this work we aim to achieve tight contact between Pd and ceria nanoparticles (NPs) by using the materials methodology of molecular doping of metals.^{18,19} This methodology enables a 3D architecture with which intimate contact between a metal matrix and a dopant—small molecules,^{20,21} polymers,^{22,23} and NPs²⁴ is created. The resulting composites exhibit unique and synergistic properties such as bioactivity,²⁵ improved catalysis,^{21,23,26} and combined ionic—electronic conductivities.²⁷ In this work, this materials methodology is used to develop synthetic conditions for the specific combination of doped ceria NPs within a catalytic Pd structure. This is a new approach in heterogeneous catalysis, as catalytic NPs are usually fixed on solid supports in 2D architectures, which in most cases are non-metallic—either carbon or metal oxides.^{28–32} The leading idea is therefore, to have a support which not only acts as a fixation method for the catalyst NPs but can also enhance its catalytic activity.^{33,34} Here we report the success of this concept which, to the best of our knowledge, was never studied, neither considered. We find that the HOR activity of the entrapped ceria in

Pd (denoted here after as CeO₂@Pd) in alkaline media is enhanced as compared to the pure Pd and commercial Pd black electrocatalyst.

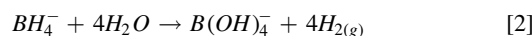
Materials and Methods

Chemicals and materials.—CeO₂ NPs (*d* = 10 nm) were purchased from US Research Nanomaterials Inc. Palladium chloride was obtained from ACROS Chemicals. Sodium borohydride (98%) was purchased from Strem chemicals. Triple distilled water with 18.2 MΩ cm^{−1} was taken from a Barnstead EasyPure UV apparatus. Pd black (Sigma Aldrich, 99.95%) was used as a reference catalytic material. Carbon black VXC MAX22 (Cabot) was the base for the gas diffusion layer (GDL) fabrication. Ni mesh (woven 100 mesh, wire diam. 0.1 mm, Alfa Aesar) was the current collector. Polytetrafluoroethylene (PTFE) suspension (60 wt% dispersion in H₂O, Sigma Aldrich) was applied as hydrophobizer. H₂ (99.999%, Maxima, Israel) was used as the fuel for the HOR measurements. KOH flakes (Bio-Lab) was obtained for the electrolyte preparation.

Synthesis method.—In general, the molecular/NP doping of metals involves reduction of the metal cation in the presence of the dopant to be entrapped. For our application, we have selected a reduction process which produces a sponge-like porous metallic structure,³⁵ to obtain high porosity and surface area of the composites, both of which are crucial characteristics for the catalytic activity. The entrapment of the CeO₂ NPs takes place along the following reduction reaction:



The sponge-like morphology was obtained by the formation of hydrogen gas from the excess of sodium borohydride according to the reaction



*Electrochemical Society Member.

^zE-mail: dario@technion.ac.il

The entrapment occurs in a simultaneous multi-step mechanism (see Scheme 1): (i) Adsorption of the dispersed nanoparticles on the

metal cations and on the surface of the forming metal crystallites; and, (ii) reduction and aggregation of the metal ions, which cause the physical entrapment of the nanoparticles in the metallic matrix. The condition for successful entrapment to occur, is to tailor the kinetics in such a way that the residence time of the NP on the forming metal nanocrystallites, is longer than the time it takes for additional Pd to form and aggregate around the NPs.

Using this method, we have prepared CeO₂@Pd catalyst composites and compare their characteristics to pure (undoped) Pd. As ceria content was found to affect the catalytic activity of the bifunctional Pd-ceria catalyst,¹³ CeO₂@Pd catalyst composites with two different compositions of ceria were prepared in order to study this effect.

CeO₂@Pd synthesis.—CeO₂ NPs (10 mg) in an aqueous solution at pH = 1.5 (25 ml) were placed in a 50 ml beaker, which was cycle-sonicated (SONICS Vibra cell probe sonicator at 130 W) for 20 min at repetitions of 2 s on and 1 s off. PdCl₂ (167 mg), HCl (230 μl) and triple distilled water (TDW, 5 ml) were placed in 10 ml beaker and stirred for 30 min. In order to disperse the CeO₂ NPs, the pH of the aqueous solution was adjusted to pH = 1.5^{36,37} by using concentrated nitric acid. The 50 ml beaker was placed under stirring and then NaBH₄ (177 mg, which represents a 5× molar excess) was added. After 30 s, the PdCl₂ solution was also added and the beaker was left under stirring for 4 min. The product was filtered under vacuum using 0.2 μm nylon filter paper (Merck Millipore), washed twice with distilled water and dried overnight under vacuum and grounded, yielding ~100 mg of CeO₂ (6.5 wt%)@Pd. For comparative purposes, pure Pd was prepared under similar conditions without the CeO₂.

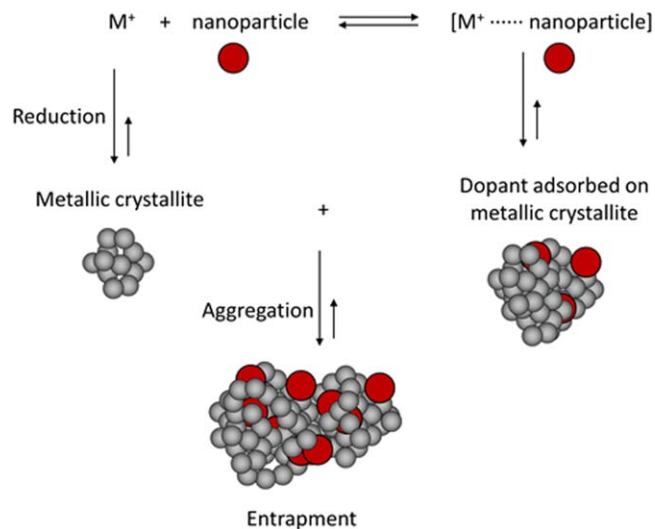
Materials characterization.—The morphology and the structural characteristics of the powders were studied by an extra high resolution scanning electron microscopy (XHR-SEM) with a FEI Magellan TM 400 I instrument fitted with an Oxford X-Max energy dispersive spectroscopy (EDS) free detector. Specific surface areas were calculated from nitrogen adsorption/desorption isotherms obtained with a Micromeritics ASAP 2020 surface area analyzer using the BET method. Powder X-ray Diffraction (XRD) measurements were carried out using Philips diffractometer (CuK_{α1} (1.5406 Å) with a step scan mode 0.02 s⁻¹). CeO₂ NPs loading (wt%) in the Pd matrix was determined from XRD pattern using Reitveld method.³⁸ HRTEM images were obtained on F20 G2 HRTEM. High-resolution HAADF STEM images and elemental mapping were obtained on FEI Themis G3 at 300 keV.

Additional experimental details.—See Supplementary Material for additional materials characterization and determination of Pd loading.

Results and Discussion

Materials characterization.—The structure of CeO₂@Pd which, on hand enables the tight encaging of the NPs on one hand, and their accessibility to reaction on the other hand, is of a sponge-like porous metallic matrix, which, throughout its volume is laced with the entrapped NPs. The cages in which the NPs are held have pore entrances which are too small for the particles to be washed out, and yet, these very pores and the general pore network of the metal, allow for gases and ions to diffuse in and out freely. Within these cages the NPs are held both by physical constrains (too narrow exit pores) and by chemisorption interaction between the ceria and the Pd, as we prove later on. Full characterization of this 3D architecture is provided.

The XRD patterns (Fig. 1a) for pure Pd and entrapped CeO₂@Pd catalysts show that both phases, metallic Pd and ceria, co-exist in the hybrid material and that they are polycrystalline, with crystallite sizes of 4–7 nm for Pd, as determined by the Scherrer equation (Table I). Table I also clearly demonstrates that the Pd crystallite



Scheme 1. Two-step mechanism of the entrapment process.

size decreases with the increase of the CeO₂ content, probably due to the adsorption of the nanoparticles on the forming Pd crystallites, which interrupts their growth. It is also seen that higher loading of CeO₂ causes a detectable change in the cell parameter of the Pd crystallites. We interpret this observation as originating from the interaction of the NPs with the Pd surface, which apparently affects the first few lattice spacings, thus affecting also the observed overall lattice parameter. The bulk chemical composition of the composites was estimated using Reitveld method³⁸ and is also shown in Table I.

HR-SEM images on the micrometric scale (Figs. 1b and S1 is available online at stacks.iop.org/JES/167/054514/mmedia), show that the pure Pd powders are composed of few-microns-size aggregates. However, the entrapment of ceria NPs changes the microstructure of the material (Figs. 1c and S1) by the reduction of the particles size, which forms the micron-size agglomerates.

SEM-EDS maps (Fig. 2) of the composite materials show that at the microscopic scale, Pd and Ce atoms are homogeneously co-distributed within the composites. STEM-EDS mapping (Fig. 3) show that direct entrapment of the ceria NPs within the palladium matrix occurs on a nanometric scale. There are also rare neighboring areas with Pd and ceria located next to each other (Fig. S2). These observations, along with the changes in the Pd crystallites size and cell parameter, demonstrate the intimate contact between the CeO₂ and the Pd, achieved in this entrapment process. From the STEM element maps (Figs. 3a–3d), it is clear that CeO₂ (red pixels) occupies the voids in the Pd phase (the dark areas surrounded by green pixels of Pd in Fig. 3b). These voids, with a characteristic size of below 50 nm, are likely the net of pores formed during the foam synthesis. The voids characteristic sizes, which are distinguishable in Fig. 3b, are in agreement with the pore size distribution curves (Fig. S3). The average pore size in the pure Pd (ca. 20 nm) is larger than the average particle sizes of CeO₂ NPs (10 nm). In addition, one can notice that the CeO₂ is located not only in between the Pd NPs, but also in areas where both Ce and Pd are present. Overlapping of Figs. 3b and 3c demonstrates that CeO₂ NPs are located within the Pd aggregates (Fig. 3d). Thus, the nanoscale EDS mapping provides a direct and conclusive experimental evidence of the entrapment of the ceria NPs within the palladium matrix. Another indication of the direct entrapment of the CeO₂ NPs within the Pd was obtained from the extended X-ray absorption fine structure (EXAFS) spectrum of the composite and its comparison to the pure Pd (Table II and Fig. S4). In the pure Pd sample, no Pd–O bonds are present, showing its stability to air oxidation, whereas for CeO₂@Pd which contains close contact Pd–O–Ce chemisorption interaction, a partial population of Pd–O bonds is clearly seen (coordination number of 0.3).

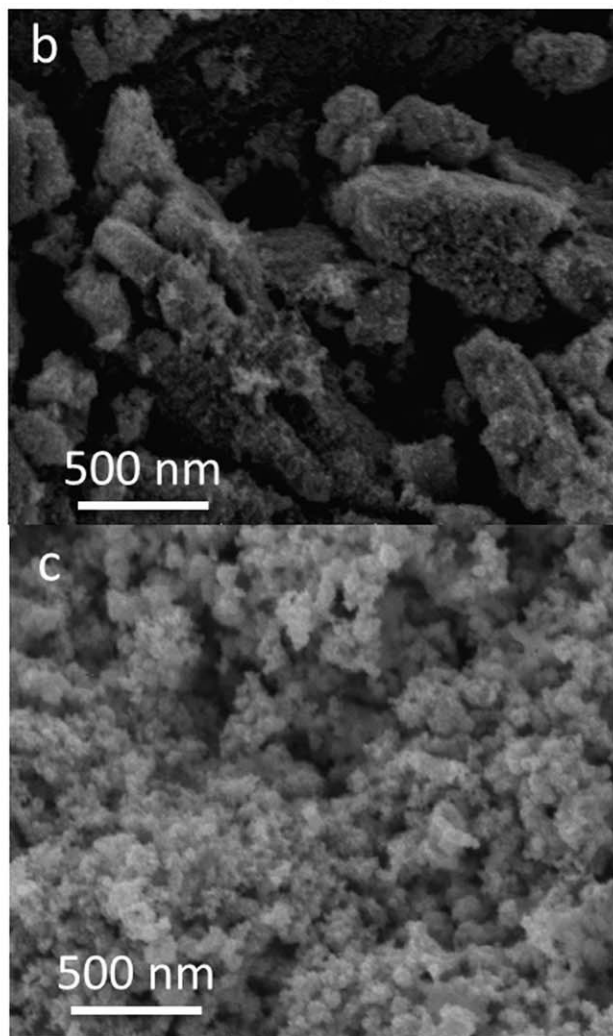
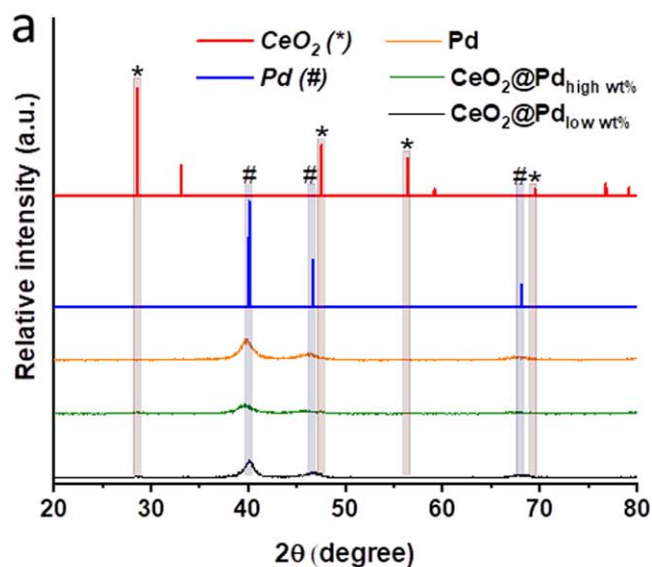


Figure 1. Materials characterization. (a): XRD for low (green) and high loading (black) CeO_2 @Pd composite and pure Pd (orange) powders. Comparison to Pd (PDF 04-003-7265) and CeO_2 (PDF 04-002-0220) references is also shown. (b), (c): HR-SEM images of pure Pd (b) and 11.6 wt% CeO_2 @Pd (c).

The Pd–Pd coordination numbers (CN), as obtained by EXAFS, of CeO_2 @Pd and of pure Pd prepared by the same method (Table II), are low compared to the CN = 12 of the FCC structure of palladium. The lower CN values are a direct indication of the open-porous structure of the entrapping metal and strongly depend on the elementary particle size.^{39,40} These lower CN values are indicative of surface defects, which in turn lead to the observed higher electrocatalytic activity compared with commercial Pd. The higher catalytic activity of CeO_2 @Pd compared to the pure Pd is due to the fact that Pd atoms near the ceria NP, at their interface, are oxidized due to the oxygen spillover ability of ceria and due to the ability of Ce^{4+} to be reduced to Ce^{3+} and oxygen vacancies.³⁴ This metal oxidation is also indicated by the Pd–O CN (Table II). The enhanced catalysis is apparently due to these Pd–O zones of the composites by their ability to weaken the Pd–H bonds,¹⁴ as is further explained in the next section. Moreover, it was shown that the transfer of OH^- from CeO_2 to Pd is accelerated in the Pd–O zones, which also contributes to the enhancement of the electrocatalytic activity.^{14,17}

We note that particle size according to EXAFS is somewhat smaller (~ 1.6 and 2.0 nm respectively, assuming the particles to be spherical) than that estimated from the Bragg reflection widths in XRD.⁴¹ Previous research has shown that of the two volume-averaged methods used here, EXAFS is more sensitive to the relative mean sizes of the nanocrystallites whilst XRD tends to be biased towards the larger crystallites.⁴² EXAFS has therefore been proposed to provide a more meaningful estimation of mean particle size. However, it should also be noted that the method is more sensitive to the effects of disorder, particularly static disorder that could arise through a significant number of metal-support interactions and which leads can lead to a reduction in this mean value of particle size.

Figure 4a shows an interconnected chain of the Pd crystallites in pure Pd catalyst. The characteristic sizes of the crystallites (ca. 5 nm, Fig. 4a) are in a good agreement with those from Table I. The TEM images (Fig. 4) confirm that at the nanometric level, the aggregates of the materials consist of a 3D network of nanometric Pd crystallites (Fig. 4a) and the CeO_2 NPs are incorporated in-between them (Fig. 4b). This network structure results in a foam-like powder with a high surface area values shown in Table III.

Table III compares the surface area, pore volume, and work function values of the entrapped and pure materials. The BET surface area of the catalysts increases in the series pure Pd < CeO_2 (6.5 wt%)@Pd < CeO_2 (11.6 wt%)@Pd. The increase in the BET surface area with the increase of the CeO_2 content might be related to two factors: (i) The increasing input of the CeO_2 surface, which was measured to be ca. $73 \text{ m}^2 \text{ g}^{-1}$, and (ii) the increase in Pd dispersion due to the stabilizing effect of CeO_2 , which is in a good agreement with the decrease of the crystallite sizes (Table I). The in situ electrochemical surface area (ECSA) values for pure Pd (ca. $31 \text{ m}^2 \text{ g}_{\text{Pd}}^{-1}$) are higher than the values obtained via N_2 adsorption (ca. $20 \text{ m}^2 \text{ g}_{\text{Pd}}^{-1}$). However, the in situ ECSA values for the entrapped catalysts are lower than the values obtained via N_2 adsorption. This observation is expected due to the fact that the ECSA values characterize specifically the surface of Pd, whereas the BET values include both Pd and CeO_2 phases. The mass-specific pore volume of pure Pd ($0.314 \text{ cm}^3 \text{ g}_{\text{cat}}^{-1}$) is higher than that of the CeO_2 @Pd composites (0.240 and $0.271 \text{ cm}^3 \text{ g}_{\text{cat}}^{-1}$ for 6.5 and 11.6 wt% of CeO_2 , respectively), which gives another straight evidence of the CeO_2 placement inside the pores of the Pd foam. This evidence is also supported by BET isotherms (Fig. S5)—showing type II isotherms^{43,44} of mesoporous materials with an average pore diameter of ~ 20 nm (Fig. S3), which are partially filled by the dispersed ~ 10 nm CeO_2 NPs. Finally, the composite materials' work function values (Table III) are similar to that for

Table I. Compositional and structural parameters of the catalysts.

Catalyst	CeO ₂ loading [wt%]	Pd crystalline size [nm]	CeO ₂ crystalline size [nm]	Pd cell parameter [Å]
Pure Pd	—	6.7 ± 0.6	—	3.892 ± 0.003
CeO ₂ @Pd	6.5 ± 0.8	6.2 ± 0.3	—	3.893 ± 0.001
	11.6 ± 0.7	4.4 ± 0.9	9.6 ± 1.2	3.920 ± 0.019

pure Pd, indicating that the basic metal-electronic features of the Pd remain unaffected after the entrapment process.

The H₂-TPR measurements of the pure Pd and CeO₂ entrapped Pd are shown in Fig. 5.

Interestingly, the H₂-TPR spectra show a negligible reduction of the catalysts (the negative values of the thermal conductivity detector (TCD) signal in the raw H₂-TPR, Fig. S6). Instead, they

reveal desorption of H₂ below 100 °C (positive TCD signal, Fig. 5), similarly to the literature data.^{45–48} The observed desorption of H₂ is due to the gas absorbed during the TCD baseline stabilization (baseline is shown in Fig. S6), which preceded the TPR step. The red arrows show the upshift of the H₂ desorption temperature for the CeO₂-entrapped catalysts as compared to the pure Pd catalyst, giving direct experimental evidence for the effect of ceria on the Pd–H_{abs}

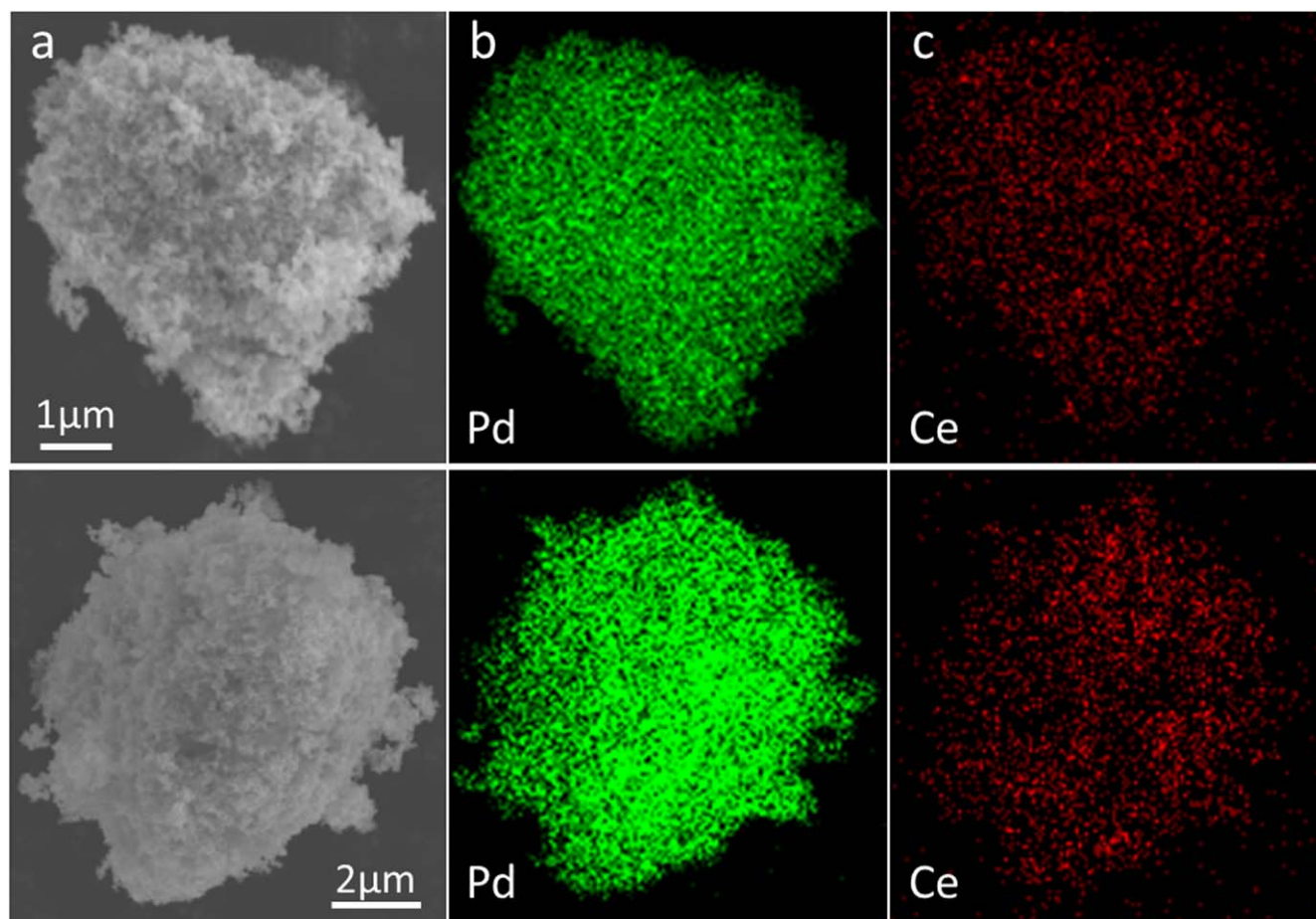


Figure 2. SEM images (a) and EDS maps ((b) Pd, (c) Ce) for the entrapped CeO₂ (6.5 wt%)@Pd (top) and CeO₂ (11.6 wt%)@Pd (bottom) catalysts.

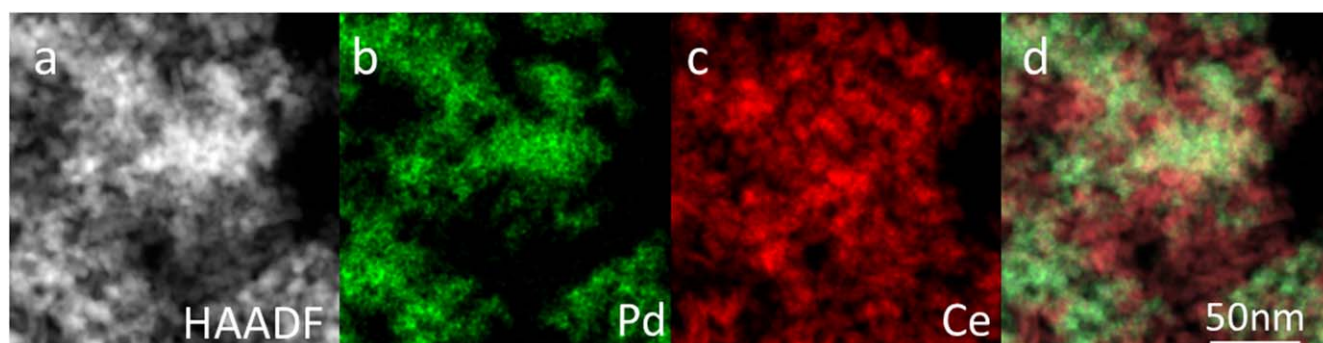


Figure 3. STEM images (a), EDS maps ((b) Pd, (c) Ce), and combined map (d) of 11.6 wt% CeO₂@Pd.

Table II. EXAFS refined structure parameters of pure Pd and CeO₂@Pd.

	Scattering path	CN	R [Å]	Scattering path	CN	R [Å]
Pure Pd	Pd–Pd	8.7	2.74	Pd–O	0	
CeO ₂ @Pd	Pd–Pd	9.4	2.74	Pd–O	0.3	1.98

CN—coordination number.

Table III. Comparison of the composition, work function and surface area of the materials.

Catalyst	Surface area		BJH pore volume [cm ³ g ⁻¹ _{cat}]	Work Function [eV]
	BET [m ² g _{cat} ⁻¹]	ECSA [m ² g _{Pd} ⁻¹]		
CeO ₂	72.3 ^{a)}	—	—	—
Pd black	40–60 ^{b)}	23.3	—	—
Pure Pd	20.0	30.7 ± 4.5	0.314	5.196 ± 0.027
CeO ₂ (6.5 wt%>@Pd	26.3	24.0 ± 1.7	0.240	5.124 ± 0.019
CeO ₂ (11.6 wt%>@Pd	52.1	33.9 ± 3.3	0.271	5.228 ± 0.026

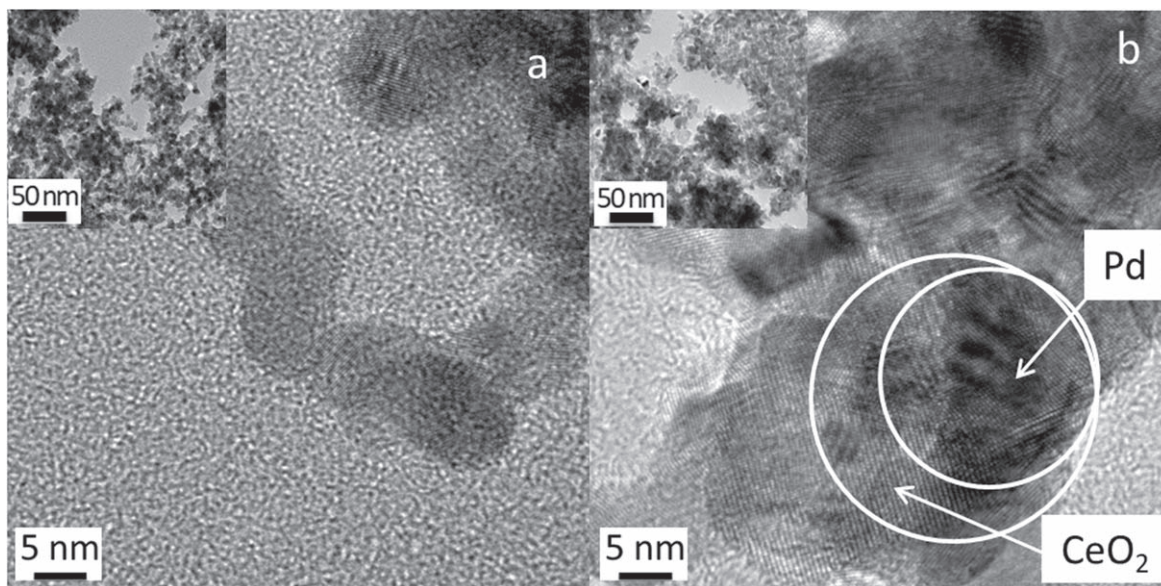
a) The value is comparable to the surface area calculated using the simple equation for spherical particles $SA_{\text{CeO}_2}(\text{m}^2 \text{g}^{-1}) = \frac{6}{d(m) \times \rho(\text{g m}^{-3})} \sim 83$, where $d = 10$ nm—average particle size of CeO₂, $\rho = 7.22$ g cm⁻³—the density of CeO₂; b) TEM-based, provided in the specification of Sigma Aldrich.

bond in the entrapped composite catalysts. The deconvolution of the spectra (dash lines, Fig. 5) also shows that the increase in the CeO₂ content results in a diversification of the absorbed hydrogen species: the number of the peaks with different desorption temperature values increases (Table SI). Thus, below ca. 120 °C, the entrapped CeO₂@Pd composites behave similarly to the 10% Pd/C-CeO₂ catalyst we reported earlier.¹⁵

Electrocatalytic activity.—Figure 6a compares the cyclic voltammogram (CV) profiles recorded for CeO₂@Pd at two ceria concentrations and pure Pd as a reference. The CV shows the typically Pd features^{49–53}: (I) under potential deposition (UPD) of atomic hydrogen from the H₂O molecule (H_{UPD})⁵⁴; (II) H₂ evolution reaction (HER)^{55–58} and Pd hydride formation (atomic hydrogen absorption)^{59,60}; (III) oxidation of the absorbed hydrogen atoms, H_{abs}, formed in the region II^{51,52}; (IV) desorption of the H_{UPD} hydrogen atoms, formed in the region I⁵⁴; (V) Pd electrooxidation⁴⁹; and (VI) PdO electrochemical reduction (used to calculate the electrochemical surface area).^{49,53,54} Additional details are provided in the Supplementary Material.

In the H_{desorption} (H_{des}) or H_{UPD} desorption region, the H_{UPD} desorption occurs at a higher overpotential value of 459 mV for pure Pd (red curve), in comparison to 374 and 389 mV for 6.5 wt% and 11.5 wt% CeO₂-entrapped catalysts, respectively. This observation could be assigned to the lower Pd–H_{des} binding energy in the CeO₂-entrapped catalysts which is in a good agreement with the work of Wang et al.⁶¹ where they found that the oxidative desorption of hydrogen is the rate-limiting step for HOR. It is interesting to note that the H_{UPD} peak shift is only detected in desorption region but not in the adsorption region. If it is caused by the change of Pd–H binding energy, the shift should be expected in both the cathodic and anodic scan. However, results show that there was no shift in adsorption region. Similar lack of shift was also seen in findings by Wang et al.⁶¹ and Miller et al.¹⁴

The higher intensity of the H_{UPD} peaks for CeO₂(6.5 wt%>@Pd compared to CeO₂(11.6 wt%>@Pd shows that the content of the entrapped CeO₂ plays a crucial role in the capacitance for hydrogen absorption. These data are also further confirmed by the H₂-temperature programmed reduction (H₂-TPR) measurements (Table SI, Fig. 5). The measurements show that the amount of H₂

**Figure 4.** TEM images of (a) pure Pd and (b) CeO₂ (11.6 wt%>@Pd. Inserts: zoom out of the images.

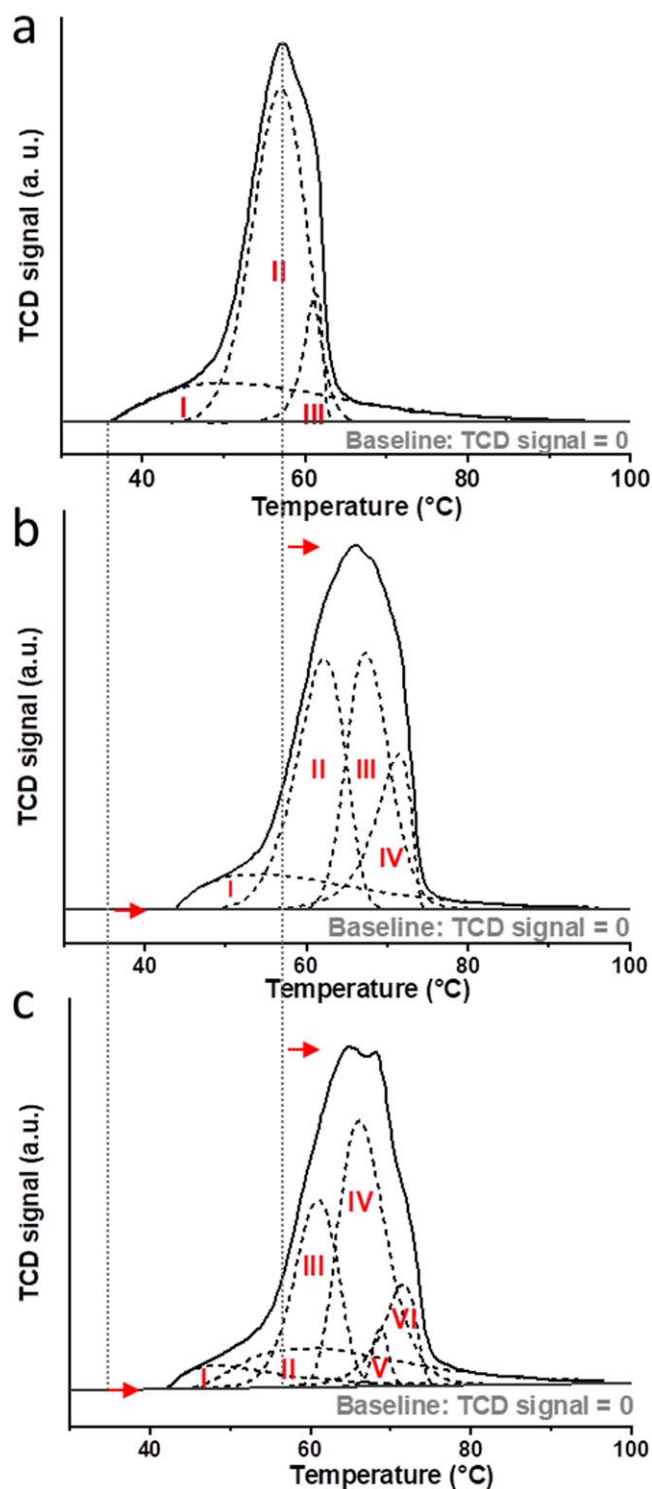


Figure 5. H_2 -TPR spectra (solid lines) and their deconvolution (dash lines) for (a) pure Pd, (b) $\text{CeO}_2(6.5 \text{ wt}\%)\text{@Pd}$, and (c) $\text{CeO}_2(11.6 \text{ wt}\%)\text{@Pd}$ composite catalysts. Arrows indicate the upshifts of the H_2 -TPR spectra. Roman numerals I-VI indicate the deconvoluted peaks, which are given in details in Table S1.

absorbed by $\text{CeO}_2(6.5 \text{ wt}\%)\text{@Pd}$, $2.63 \text{ mmol}_{\text{H}_2} \text{g}^{-1}_{\text{Pd}}$, is higher than that for the $\text{CeO}_2(11.6 \text{ wt}\%)\text{@Pd}$ catalyst, $2.42 \text{ mmol}_{\text{H}_2} \text{g}^{-1}_{\text{Pd}}$, and that both entrapped $\text{CeO}_2\text{@Pd}$ catalysts show higher absorption capacitance as compared to that measured for pure Pd ($2.20 \text{ mmol}_{\text{H}_2} \text{g}^{-1}_{\text{Pd}}$).

Similarly to our previous results,¹⁵ we assume, that due to the significantly higher affinity of the $\text{CeO}_2\text{@Pd}$ catalysts to hydrogen

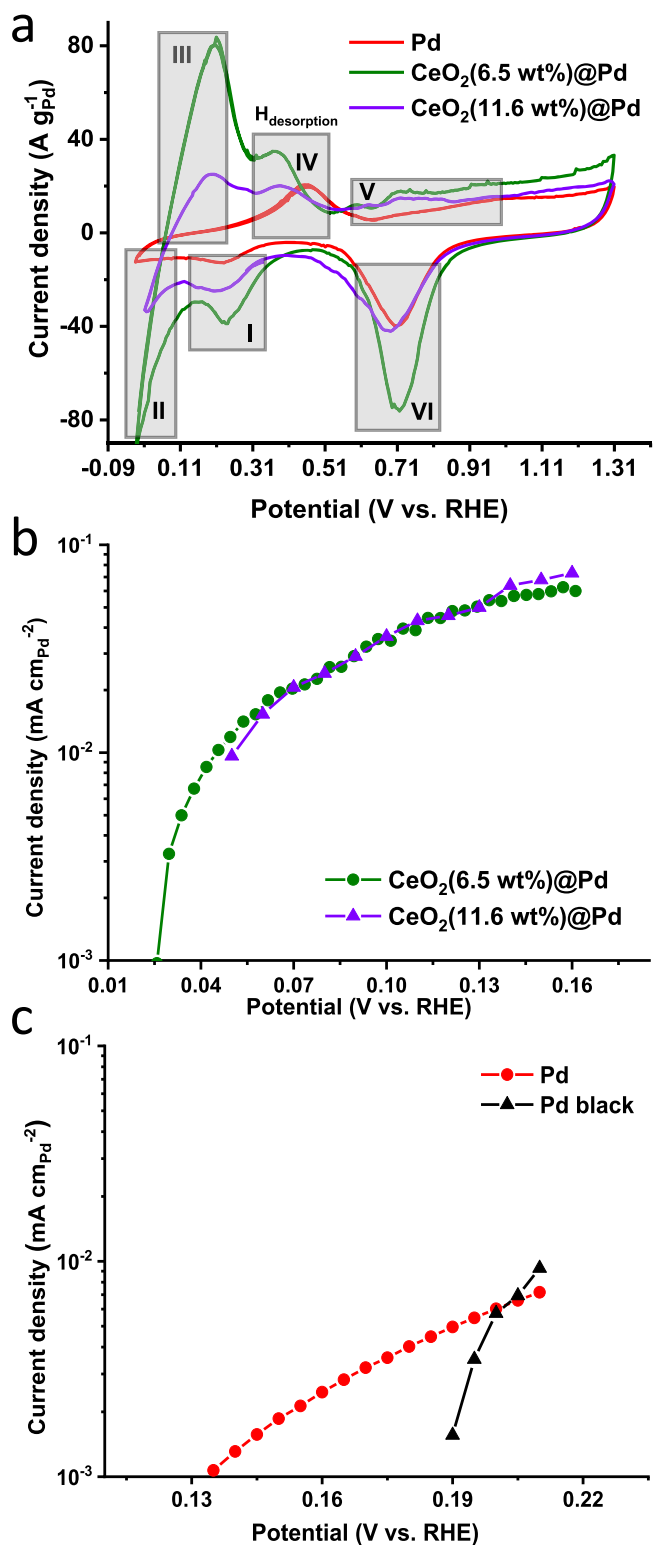


Figure 6. (a) Comparison of the mass-normalized cyclic voltammograms for the $\text{CeO}_2\text{@Pd}$ composites and its comparison with that of pure Pd. Polarization curves of HOR (b) for the entrapped $\text{CeO}_2\text{@Pd}$ materials, and (c) for pure Pd catalysts. The current values were normalized to the ECSA values presented in Table I.

absorption as compared to pure Pd, they might show lower binding energy to the hydrogen adsorption, which in turn has a positive effect on the Volmer step of HOR (Scheme S1).⁵⁷ Consequently, the entrapped composite catalysts demonstrate more than one order of

magnitude higher surface-specific activity in hydrogen electrooxidation reaction. For instance, the catalytic activity at the potential value of -0.75 V reaches 0.06 and 0.073 mA cm⁻²_{Pd} for CeO₂(6.5 wt%)/Pd and CeO₂(11.6 wt%)/Pd, respectively, compared to only 0.0025 mA cm⁻²_{Pd} for the pure Pd catalyst at the same potential (Figs. 6b and 6c).

Conclusions

A new type of electrocatalytic heterogeneous catalyst based on ceria entrapped into palladium metal catalyst was developed. TEM-SEM-EDS maps of the resulting composite materials show that at the microscopic scale Pd and Ce atoms are homogeneously co-distributed within the composites, while STEM-EDS mapping shows that direct entrapment of the ceria nanoparticles within the palladium matrix occurs on a nanometric scale. These observations, along with the changes in the Pd crystallites size and cell parameter, demonstrate the intimate contact between the CeO₂ and the Pd, achieved in this entrapment process.

The CeO₂@Pd composite catalyst clearly shows the significant effect of the intimate contact between the two components leading to their improved catalytic properties towards the electrocatalytic hydrogen oxidation reaction in alkaline medium. The crucial role of the entrapped CeO₂ to improve the electrocatalytic activity of the Pd was further confirmed by H₂-TPR measurements as well as by polarization curves of HOR, which clearly show the significant increase of the current densities of the entrapped CeO₂@Pd composite catalysts.

We believe that this new type of synthesis of electrocatalytic materials may be expanded to other oxide materials and other metal electrocatalysts. As proven here with the entrapped CeO₂@Pd system, we believe that this new type of intimate contact at a nanometric level between oxides and metallic catalysts may impart significantly higher catalytic properties to the entrapped composite electrocatalysts. Such materials may impart significant advantages to the next generations of fuel cells, electrolyzers, batteries, and other electrochemical devices where the electrocatalytic activity of the electrodes is of crucial importance.

Acknowledgments

This work was partially funded by the Nancy & Stephan Grand Technion Energy Program (GTEP); by the European Union's Horizon 2020 research and innovation program [grant No. 721065]; by the Ministry of Science, Technology & Space of Israel through grant No. 3-12948; by the Israel Science Foundation (ISF) [grant No. 1481/17]; by the Russell Berrie Nanotechnology Institute, Technion; by the Ministry of National Infrastructure, Energy and Water Resources of Israel [grant No. 3-13671]. The authors would also like to acknowledge the financial support of Melvyn & Carolyn Miller Fund for Innovation, as well as the support of Planning & Budgeting Committee / ISRAEL Council for Higher Education (CHE) and Fuel Choice Initiative (Prime Minister Office of ISRAEL), within the framework of "Israel National Research Center for Electrochemical Propulsion (INREP)". G.S.G. also acknowledges support from the Gruenbaum chair in Materials Engineering. We thank Barak Menagen for taking part in the EXAFS measurements, and Evgeniy Mervinetskiy and Prof. Lioz Etgar for support in work function measurements.

References

1. E. S. Davydova, S. Mukerjee, F. Jaouen, and D. R. Dekel, *ACS Catal.*, **8**, 6665 (2018).
2. D. R. Dekel, *Curr. Opin. Electrochem.*, **12**, 182 (2018).
3. E. S. Davydova, F. D. Speck, M. T. Y. Paul, D. R. Dekel, and S. Cherevko, *ACS Catal.*, **9**, 6837 (2019).
4. D. R. Dekel, in *ECS Transactions*, **50**, 2051 (2013).
5. D. R. Dekel, *J. Power Sources*, **375**, 158 (2018).
6. E. Davydova, J. Zaffran, K. Dhaka, M. Toroker, and D. Dekel, *Catalysts*, **8**, 454 (2018).

7. S. Maurya et al., *ACS Catal.*, **8**, 9429 (2018).
8. W. Sheng, H. A. Gasteiger, and Y. Shao-Horn, *J. Electrochem. Soc.*, **157**, B1529 (2010).
9. K. Elbert, J. Hu, Z. Ma, Y. Zhang, G. Chen, W. An, P. Liu, H. S. Isaacs, R. R. Adzic, and J. X. Wang, *ACS Catal.*, **5**, 6764 (2015).
10. C. Lafforgue, M. Chatenet, L. Dubau, and D. R. Dekel, *ACS Catal.*, **8**, 1278 (2018).
11. N. Ramaswamy, S. Ghoshal, M. K. Bates, Q. Jia, J. Li, and S. Mukerjee, *Nano Energy*, **41**, 765 (2017).
12. D. Strmcnik, M. Uchimura, C. Wang, R. Subbaraman, N. Danilovic, D. van der Vliet, A. P. Paulikas, V. R. Stamenkovic, and N. M. Markovic, *Nat. Chem.*, **5**, 300 (2013).
13. H. A. Miller et al., *Nano Energy*, **33**, 293 (2017).
14. H. A. Miller, A. Lavacchi, F. Vizza, M. Marelli, F. Di Benedetto, F. D'Acapito, Y. Paska, M. Page, and D. R. Dekel, *Angew. Chemie - Int. Ed.*, **55**, 6004 (2016).
15. M. Bellini et al., *ACS Appl. Energy Mater.*, **2**, 4999 (2019).
16. V. Yarmiyayev, M. Alesker, A. Muzikansky, M. Zysler, and D. Zitoun, *J. Electrochem. Soc.*, **166**, F3234 (2019).
17. H. Yu, E. S. Davydova, U. Ash, H. A. Miller, L. Bonville, D. R. Dekel, and R. Maric, *Nano Energy*, **57**, 820 (2019).
18. D. Avnir, *Acc. Chem. Res.*, **47**, 579 (2014).
19. D. Avnir, *Adv. Mater.*, 1706804 (2018).
20. H. Behar-Levy and D. Avnir, *Chem. Mater.*, **14**, 1736 (2002).
21. G. E. Shter, H. Behar-Levy, V. Gelman, G. S. Grader, and D. Avnir, *Adv. Funct. Mater.*, **17**, 913 (2007).
22. H. Behar-Levy, G. E. Shter, G. S. Grader, and D. Avnir, *Chem. Mater.*, **16**, 3197 (2004).
23. L. Shapiro and D. Avnir, *Chem. Cat. Chem.*, **5**, 2195 (2013).
24. N. Ralbag, I. Felner, and D. Avnir, *Phys. Rev. B*, **99**, 064411 (2019).
25. B. Menagen, R. Pedahzur, and D. Avnir, *Sci. Rep.*, **7**, 4161 (2017).
26. L. Shapiro, M. Driess, and D. Avnir, *Chem. Cat. Chem.*, **7**, 2033 (2015).
27. N. Ralbag et al., *Matter*, **1**, 959 (2019).
28. J. B. Park, J. Graciani, J. Evans, D. Stacchiola, S. D. Senanayake, L. Barrio, P. Liu, J. F. Sanz, J. Hrbek, and J. A. Rodriguez, *J. Am. Chem. Soc.*, **132**, 356 (2010).
29. M. Haruta, *Chem. Rec.*, **3**, 75 (2003).
30. M. L. Toebes, J. A. van Dillen, and K. P. de Jong, *J. Mol. Catal. A: Chem.*, **173**, 75 (2001).
31. J. A. Rodriguez, P. Liu, X. Wang, W. Wen, J. Hanson, J. Hrbek, M. Pérez, and J. Evans, *Catal. Today*, **143**, 45 (2009).
32. M. Alesker, M. Page, M. Shviro, Y. Paska, G. Gershinsky, D. R. Dekel, and D. Zitoun, *J. Power Sources*, **304**, 332 (2016).
33. M. Haruta, *Cattech*, **6**, 102 (2002).
34. Z. A. Qiao, Z. Wu, and S. Dai, *Chem. Sus. Chem.*, **6**, 1821 (2013).
35. K. S. Krishna, C. S. S. Sandeep, R. Philip, and M. Eswaramoorthy, *ACS Nano*, **4**, 2681 (2010).
36. A. Sehgal, Y. Lalatonne, J. F. Berret, and M. Morvan, *Langmuir*, **21**, 9359 (2005).
37. M. Nabavi, O. Spalla, and B. Cabane, *J. Colloid Interface Sci.*, **160**, 459 (1993).
38. H. M. Rietveld, *J. Appl. Crystallogr.*, **2**, 65 (1969).
39. A. I. Frenkel, A. Yevick, C. Cooper, and R. Vasic, *Annu. Rev. Anal. Chem.*, **4**, 23 (2011).
40. A. Witkowska, A. Di Cicco, and E. Principi, *Phys. Rev. B—Condens. Matter Mater. Phys.*, **76**, 104110 (2007).
41. A. M. Beale and B. M. Weckhuysen, *Phys. Chem. Chem. Phys.*, **12**, 5562 (2010).
42. Calvin, S. X. Luo, C. Caragianis-Broadbridge, J. K. McGuinness, E. Anderson, A. Lehman, K. H. Wee, S. A. Morrison, and L. K. Kurihara, *Appl. Phys. Lett.*, **87**, 233102 (2005).
43. M. Thammes, K. Kaneko, A. V. Neimark, J. P. Olivier, F. Rodriguez-Reinoso, J. Rouquerol, and K. S. W. Sing, *Pure Appl. Chem.*, **87**, 1051 (2015).
44. A. Chakraborty and B. Sun, *Appl. Therm. Eng.*, **72**, 190 (2014).
45. K.-L. Loh and Y.-N. Tang, *J. Chinese Chem. Soc.*, **34**, 231 (1987).
46. S. Ohno, M. Wilde, and K. Fukutani, *J. Phys. Chem. C*, **119**, 11732 (2015).
47. A. Aznárez, A. Gil, and S. A. Korili, *RSC Adv.*, **5**, 82296 (2015).
48. J. A. Konvalinka and J. F. Scholten, *J. Catal.*, **48**, 374 (1977).
49. G. Macfie, A. Cooper, and M. F. Cardosi, *Electrochim. Acta*, **56**, 8394 (2011).
50. M. M. Jaksic, B. Johansen, and R. Tunold, *Int. J. Hydrogen Energy*, **18**, 111 (1993).
51. C. Gabrielli, P. P. Grand, A. Lasia, and H. Perrot, *J. Electrochem. Soc.*, **151**, A1937 (2004).
52. V. C. Diculescu, A.-M. Chiorcea-Paquim, O. Corduneanu, and A. M. Oliveira-Brett, *J. Solid State Electrochem.*, **11**, 887 (2007).
53. S. Henning, J. Herranz, and H. A. Gasteiger, *J. Electrochem. Soc.*, **162**, 178 (2015).
54. A. V. Uluc, J. M. C. Mol, H. Terryn, and A. J. Böttger, *J. Electroanal. Chem.*, **734**, 53 (2014).
55. J. Wei, M. Zhou, A. Long, Y. Xue, H. Liao, C. Wei, and Z. J. Xu, *Nano-Micro Lett.*, **10**, 75 (2018).
56. Sarkar and S. C. Peter, *Inorg. Chem. Front.*, **5**, 2060 (2018).
57. P. Quaino and E. Santos, *Langmuir*, **31**, 858 (2015).
58. N. Pentland, J. O. Bockris, and E. Sheldon, *J. Electrochem. Soc.*, **104**, 182 (1957).
59. B. Wickman, M. Fredriksson, L. Feng, N. Lindahl, J. Hagberg, and C. Langhammer, *Phys. Chem. Chem. Phys.*, **17**, 18953 (2015).
60. F. Lewis, *Platin. Met. Rev.*, **4**, 132 (1960), <https://technology.matthey.com/article/4/4/132-137/>.
61. Y. Wang, G. Wang, G. Li, B. Huang, J. Pan, Q. Liu, J. Han, L. Xiao, J. Lu, and L. Zhuang, *Energy Environ. Sci.*, **8**, 177 (2015).